Mass-Constrained Thermal Protection for Mask-Delivery Multirotor UAVs in Fireground Rescue Operations: A Material Synthesis and Analytical Feasibility Study

[Author name(s)]

Abstract

Drones flown near active fires must survive radiant heat, hot plumes and thin air, yet the obvious fix—wrapping the aircraft in insulation—fails, because hover power rises with the 3/2 power of mass and every gram of shielding is paid for in flight time. Existing reviews compare thermal protection materials by conductivity alone, which ignores this mass coupling. This study synthesises property and degradation data from 28 published sources and evaluates them inside an analytical framework covering radiant loading, transient conduction, mass-penalty scaling and rotor performance in heated air. Its central contribution is a mass-specific figure of merit, $\Phi = 1/(k\rho)$, giving thermal resistance per unit areal mass; because Φ is independent of layer thickness, it ranks candidate systems on a basis that thickness cannot distort. Ranked this way the ordering changes sharply. Ceramic fiber-functionalized silica aerogel (CFSA) outperforms bare carbon-fiber-reinforced polymer by a factor of 316, a Si–B phenolic aerogel by 61 and low-density carbon–carbon by 29, whereas a dense ceramic barrier coating gains only a factor of 2.0 and is therefore justified solely as a micrometre-scale radiative film. A worked sizing case shows a $0.5\,\mathrm{m^2K/W}$ barrier around a $0.05\,\mathrm{m^2}$ avionics bay on a 2 kg platform costs 6.1% of gross mass and 8% of endurance in CFSA, but 31.9% and 34% in the phenolic system. A separate result shows shaft speed and hover power both scale as $\sqrt{T}$, rising 62% at 500 °C. The analysis supports component-specific rather than uniform protection.

Keywords: thermal protection systems; silica aerogel; multirotor UAV; firefighting robotics; materials selection; hover endurance.

1 Introduction and Objective

Smoke inhalation, not flame, is what disables most fireground survivors in the minutes before a rescue team can reach them, and that window is exactly where aerial platforms already operate: supplying infrared imagery of the fire front, tracking its spread, and surveying damaged structures without exposing crews [1, 27]. A multirotor tasked with actually placing protective masks in survivors' hands, rather than only observing from a safe standoff, has to close that distance — loitering directly over a collapsed stairwell or hovering inside a smoke-filled room long enough to release its payload. That mission profile means accepting flame impingement, sustained radiant flux, and immersion in convective plumes for longer and at closer range than a surveillance pass requires [2, 11], and the polymer matrices that keep a small multirotor light enough to carry a useful mask payload begin to fail within minutes under that exposure [6, 28].

Two failure paths dominate. Thermally, flight controllers, sensors, the payload-release mechanism, and lithium-polymer cells all sustain irreversible damage above roughly 70 °C [27, 28]. Aerodynamically, hot air is thin air, so a rotor inside a plume produces less thrust at the same shaft speed, forcing higher RPM and higher current—which adds Joule heating to an already hot vehicle [2, 7]. Neither path is solved by simply adding insulation, because on a mask-delivery platform every gram of shielding is a gram not available for mask cargo, and added mass degrades endurance faster than it buys protection [10, 12].

The objective of this study is therefore to determine *which* thermal protection materials a small multirotor can actually afford to carry without crowding out its life-saving payload, and where on the vehicle each belongs, by treating protection as a constrained optimisation shared with payload capacity rather than a material-selection exercise in isolation.

2 Literature Review

Unmanned aerial vehicles that operate near active firegrounds face a punishing thermal environment: intense radiative flux, occasional direct flame contact, and convective plumes that can compromise both structural integrity and onboard functionality [1,2,27]. Most small multirotor UAVs are built from thermoplastics, thermosets, or carbon-fiber-reinforced polymer (CFRP), materials chosen mainly for their favorable strength-to-weight ratios [3,4]. The trade-off is thermal tolerance. Glycol-modified PET (PETG), for instance, begins to soften near its glass transition temperature of roughly 80°C [3]; aramid-reinforced thermoplastics hold up well against physical impact but offer almost no thermal insulation [5]; and CFRP airframes start to suffer matrix resin oxidation and delamination once temperatures climb past 300°C [6]. Beyond outright material degradation, elevated ambient heat also warps propellers, twists blades, and creates structural hotspots — effects that shorten service life and raise the risk of aerothermoelastic flutter [7–10].

These thermal limits have pushed researchers toward ultra-low-density insulating systems. Aerogel composites, with thermal conductivities as low as 0.018–0.040 W/m·K, have already found their way into platforms such as the FireDrone [11], medical delivery drones [12], and automotive battery packs [18], where they help keep internal temperatures below critical thresholds even under severe thermal loading [19]. The

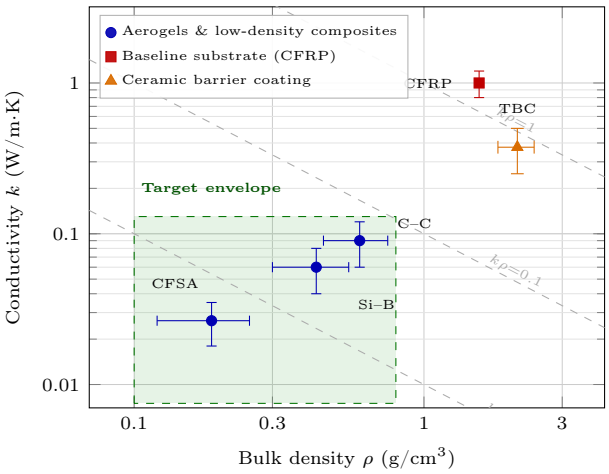

Figure 1: Design space of thermal conductivity against bulk density compiled from reviewed literature.

catch with aerogels has always been their mechanical brittleness, and much of the recent work is aimed squarely at that weakness. Ceramic fiber-functionalized silica aerogels (CFSA) [13], ceramizable Si–B hybrid phenolic aerogels [14], elastic ceramic-carbon aerogels [15], and load-bearing carbon/carbon (C–C) composites [16,17,20] each attempt to graft ceramic-like resilience onto an aerogel's inherently low density, and collectively they push operational stability as high as 1800°C while resisting flame erosion.

Bulk insulation is only part of the picture, though. Surface coatings and thermal barrier treatments play a complementary role, governing radiative boundary conditions and oxidation kinetics at the material surface [21,22]. Research into endothermic pyrolysis [25], high-temperature epoxy degradation [23], arc-jet testing of modified resins [24], and hydrophobic polyimide composites [26] has repeatedly surfaced the same underlying tension among insulation efficiency, substrate adhesion, and anti-vibration resistance — gains in one area tend to come at the expense of another. For sensitive onboard electronics, passive phase-change materials and thermochemical energy storage system serve as crucial secondary heat sinks [27, 28].

A critical gap across existing literature is that thermal protection candidate systems are evaluated primarily by thermal conductivity (k), neglecting the substantial flight endurance penalties associated with added shield mass on multirotor platforms. Evaluating candidate systems within a unified design space of conductivity against bulk density (Fig. 1) demonstrates the necessity of a mass-specific evaluation metric.

3 Methodology

The model is deliberately reduced. Its purpose is not to predict a temperature field but to establish which material classes can meet a protection requirement without consuming the endurance budget.

Assumptions. Conduction is one-dimensional and normal to the surface, valid for a thin shell whose in-plane dimensions exceed its thickness. Properties are constant over the exposure, which understates ceramizing systems [14, 17]. The flame is a grey isotropic emitter. Rotor behaviour follows momentum theory at fixed thrust coefficient.

Radiant loading. For a component at standoff d from a core of radiating area A_f,

$$q'' = \frac{\varepsilon_\mathrm{f}\,\sigma A_\mathrm{f}\left(T_\mathrm{src}^4 - T_\mathrm{surf}^4\right)}{4\pi d^2}, \tag{1}$$

with $\sigma = 5.670\times10^{-8}\,\mathrm{W/m^2K^4}$. The $4\pi d^2$ term is the isotropic point-source limit; for a plume subtending a large solid angle it becomes a lower bound. Only the absorbed fraction drives conduction, so across a barrier of thickness Δx at steady state,

$$\Delta T = (1-\alpha_r)\,q''\,\Delta x/k, \tag{2}$$

where α_r is spectral reflectance over the source band. Raising α_r lowers the absorbed fraction. The design target is spectrally selective: high reflectance in the near-infrared where flames radiate, high emittance at the surface's own temperature so absorbed energy is re-radiated [21, 22].

Transient response. A fireground pass is transient, governed by $\partial T/\partial t = \alpha\,\partial^2 T/\partial x^2$ with diffusivity $\alpha = k/\rho c_p$. Using the Fourier number $\mathrm{Fo} = \alpha t/L^2$ and taking significant inner-face response at $\mathrm{Fo}\approx 0.1$–0.3, the time for the inner face of a barrier of thickness L to reach $T_\mathrm{crit}\approx 70\,^\circ\mathrm{C}$ is

$$t_\mathrm{delay} \approx \mathrm{Fo}\,L^2\rho\,c_p/k. \tag{3}$$

The window lengthens with volumetric heat capacity ρc_p and shortens with k, which is why phase-change inserts complement a low-k shell [27, 28]: they raise ρc_p without raising k.

Figure of merit. Let a barrier deliver areal resistance $R'' = L/k$ at areal mass $m'' = \rho L$. Their ratio,

$$\Phi = R''/m'' = (L/k)/(\rho L) = 1/(k\rho), \tag{4}$$

is independent of L and gives thermal resistance purchased per unit areal mass. On logarithmic k–ρ axes, contours of constant Φ are straight lines of slope -1.

Mass penalty. Momentum theory gives induced hover power $P_\mathrm{h} = (Mg)^{3/2}/\sqrt{2\rho_\mathrm{air}A_\mathrm{rot}}$, so for fixed battery energy E and efficiency η,

$$t_\mathrm{flight} = E\eta/P_\mathrm{h} \;\propto\; M^{-3/2}. \tag{5}$$

With shield mass fraction $\mu = m_\mathrm{shield}/M_0$, retained endurance is $(1+\mu)^{-3/2}$.

Rotor performance in heated air. At constant pressure $\rho_\mathrm{air} = P_\mathrm{atm}/R_\mathrm{sp}T$, and thrust $T_\mathrm{h} = C_T\rho_\mathrm{air}n^2D^4$. Holding $T_\mathrm{h} = Mg$,

$$\frac{n_\mathrm{hot}}{n_\mathrm{amb}} = \sqrt{\frac{T_\mathrm{hot}}{T_\mathrm{amb}}} = \frac{P_\mathrm{h,hot}}{P_\mathrm{h,amb}}, \tag{6}$$

the final equality following because $P_\mathrm{h}\propto\rho_\mathrm{air}^{-1/2}$.

4 Results and Discussion

4.1 Collated properties and ranking

Table 1 lists property ranges from the reviewed sources with Φ from Eq. (4), normalised to unprotected CFRP

Table 1: Property ranges collated from the reviewed literature (left), the resulting mass-specific merit $\Phi_r = \Phi/\Phi_{\mathrm{CFRP}}$, and the sizing outcome (right) for a barrier resistance $R'' = 0.5\,\mathrm{m^2K/W}$ over a $0.05\,\mathrm{m^2}$ avionics envelope on a 2.0 kg platform. All derived quantities use range midpoints.

	Collated properties				Sizing outcome at $R'' = 0.5\,\mathrm{m^2K/W}$				
Material system	ρ (g/cm^3)	k (W/m·K)	$T_{\max}$ (°C)	Φ_r	L (mm)	m'' (kg/m^2)	m_{sh} (kg)	μ (%)	t/t_0
CFSA silica aerogel	0.12–0.25	0.018–0.035	1000	316	13.3	2.5	0.12	6.1	0.92
Si–B phenolic aerogel	0.30–0.55	0.040–0.080	1200	61	30.0	12.8	0.64	31.9	0.66
Low-density C–C	0.45–0.75	0.060–0.120	1800	29	45.0	27.0	1.35	67.5	0.46
Ceramic TBC layer	1.80–2.40	0.250–0.500	>1500	2.0	187.5	393.8	19.7	984	infeasible
Unprotected CFRP	1.50–1.60	0.800–1.200	300	1.0	500.0	775.0	38.8	1938	infeasible

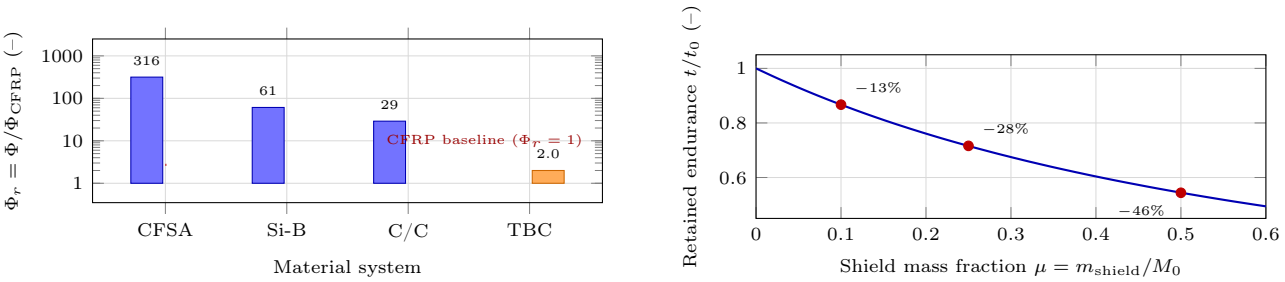

(a) Mass-specific insulation merit

(b) Endurance penalty of added shield mass

Figure 2: Validation of the selection criterion. (a) Mass-specific thermal resistance from Eq. (4) at the midpoints of Table 1, measured from the CFRP baseline on a logarithmic ordinate. (b) Retained hover endurance from Eq. (5).

at range midpoints. Ranges are reported as ranges deliberately: values scatter because measurement standards and test temperatures differ across studies.

Figure 1 plots these ranges on logarithmic axes with iso-merit contours. The separation is larger than the property scatter, which matters more than its size. CFRP sits in the upper right at $k \approx 1.0\,\mathrm{W/m \cdot K}$ and $\rho \approx 1.55\,\mathrm{g/cm^3}$: a structural material that happens to conduct heat efficiently into the payload bay. The ceramic barrier layer improves conductivity 2.7-fold but raises density 35%, so it crosses only one contour and stays near $k\rho \approx 0.8$. The three low-density systems sit two contours lower, and no range overlaps between groups—so the ranking survives the measurement scatter.

Figure 2(a) ranks the same result. CFSA delivers 316 times the thermal resistance per unit areal mass of bare CFRP, the Si–B aerogel 61 times and low-density C–C 29 times; the ceramic layer manages 2.0. That last figure is the operative one for coating design: a barrier coating cannot serve as bulk insulation at any practical thickness, and belongs on the vehicle only as a micrometre-scale radiative treatment, where Eq. (2) rather than Eq. (3) governs its usefulness.

4.2 Sizing case

Figure 2(b) shows why the ranking matters operationally: retained endurance $(1+\mu)^{-3/2}$ is concave, so 10% added mass costs 13% of flight time, 25% costs 28% and 50% costs 46%. Combining this with Table 1, consider an avionics envelope of $A = 0.05\,\mathrm{m^2}$ on an unshielded platform of $M_0 = 2.0\,\mathrm{kg}$ requiring $R'' = 0.5\,\mathrm{m^2K/W}$. Since $L = kR''$ and $m'' = \rho L$, thickness and shield mass follow directly from the midpoint properties (Table 1, right).

Only the CFSA shell is comfortable: 13 mm of wall and 8% of endurance. The Si–B system is viable but expensive at a third of the airframe mass, which argues for using it selectively on faces exposed to direct impingement rather than around the whole enclosure. Low-density C–C is not competitive as a pure insulator here, though that understates its value, since it also carries structural load otherwise duplicated in CFRP. The last two rows make the point quantitatively rather than rhetorically: at this target both would exceed the airframe mass several times over.

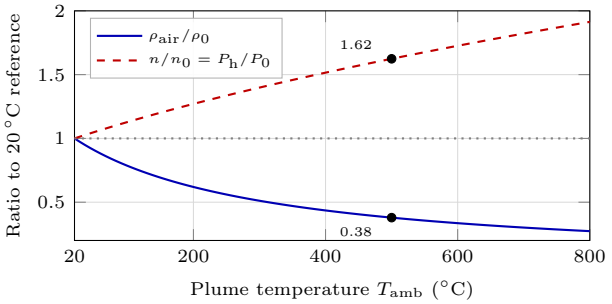

Figure 3: Air density, required shaft speed and induced hover power in a heated plume, from Eq. (6). At 500 °C the rotor must turn 62% faster and absorb 62% more power for the same lift.

For a mask-delivery airframe this comparison is not academic. The 0.52 kg difference in shield mass between the Si–B system and CFSA — roughly a quarter of the platform's gross mass — is cargo capacity either spent on insulation or available to carry masks to survivors. On a 2.0 kg platform, that difference is the gap between a token payload and a sortie large enough to matter, which is why CFSA is treated as the default choice in Section 4.4 rather than one option among several of comparable merit.

4.3 Propulsion penalty in the plume

Figure 3 evaluates Eq. (6) to 800 °C. Density falls as T^{-1} while shaft speed—and, identically, induced hover power—rises as $\sqrt{T}$. At 500 °C density drops to 38% of ambient and both speed and power rise 62%. Two consequences follow. Thrust margin must be sized for the plume, not for the pad: a vehicle hovering at 62% of maximum thrust at ambient has no reserve at 500 °C. And the extra current is dissipated at the motors, immediately adjacent to the composite booms, making that interface a heat source in its own right rather than only a conduction path from outside.

4.4 Recommended layout

Each region of the vehicle has a different dominant loading term, so the appropriate material follows from which term dominates. *Avionics, battery, and payload-release bay:* conduction-limited and the only region with a hard ceiling—housing the flight controller, cells, and the mask-release actuator inside a single CFSA shell sized as in Table 1, with phase-change or thermochemical inserts [27, 28] raising the effective ρc_p of Eq. (3); consolidating these heat-sensitive components into one enclosure avoids paying the shield-mass penalty twice. *Rotor blades:* radiation-limited and intolerant of section change—only a spectrally selective film of order 20–50 μm [21, 22] is admissible, since Eq. (4) shows a thicker layer buys negligible resistance for substantial mass. *Structural booms:* low-density C–C [20] or polyimide composites with hydrophobic coatings [26] hold rigidity to about 500 °C, the case where the poor insulator ranking of C–C is offset by the structural mass it replaces. *Motor mounts:* ceramic isolators [24] break the internal conduction path identified above, and must tolerate vibration—precisely the trade characterised by arc-jet testing in [24].

5 Conclusions and Limitations

For a UAV whose mission is to fly masks to survivors rather than only photograph them, survivability on the fireground is a mass-allocation problem before it is a materials problem, because payload capacity and thermal protection draw on the same mass budget. Ranking candidates by mass-specific thermal resistance rather than conductivity reorders them substantially: CFSA outperforms bare CFRP by 316, the Si–B system by 61 and low-density C–C by 29, while a dense ceramic barrier gains only 2.0 and is justified solely by its radiative and oxidation behaviour. The sizing case shows a 0.5 $\mathrm{m^2K/W}$ barrier around a small avionics and payload-release bay is affordable in aerogel at 6.1% of gross mass and 8% of endurance, and not affordable in any denser system; choosing CFSA over the next-best Si–B system alone frees roughly 0.52 kg, about a quarter of the platform's gross mass, that can be redirected from shielding to mask cargo. Alongside this, shaft speed and hover power both rise as $\sqrt{T}$, so thrust margin must be reserved for plume immersion rather than consumed at ambient conditions.

Several limitations bound these conclusions. Property values come from studies using different specimens, standards and test temperatures, so Table 1 is indicative rather than a qualified database. The constant-property treatment penalises ceramizing systems [14, 17]; a transient formulation with temperature-dependent properties would likely narrow the CFSA–Si–B gap. Convective coupling to the plume, joint conduction, the vibration durability of a thin aerogel shell, and the added mass and aerodynamic drag of the mask canister and release mechanism itself lie outside the present scope. Experimental validation of an assembled stack—aerogel shell, selective coating, PCM insert, and payload module together—under representative flux and vibration remains the necessary next step.

References

[1] T. B. Alappatt *et al.*, "Design and Analysis of Fire Fighting Drone," *Lect. Notes Mech. Eng.*, pp. 1015–1033, 2021.

[2] D. Aláez, M. Prieto, J. E. Villadangos, and J. J. Astrain, "Towards a Heat-Resistant Tethered Micro-Aerial Vehicle for Structure Fire Sensing," *Appl. Sci.*, vol. 15, no. 5, p. 2388, 2025.

[3] M. Baltić *et al.*, "PETG as an Alternative Material for the Production of Drone Spare Parts," *Polymers*, vol. 16, no. 21, p. 2976, 2024.

[4] A. Kantaros, C. Drosos, M. Papoutsidakis, E. Pallis, and T. Ganetsos, "Composite Filament Materials for 3D-Printed Drone Parts," *Materials*, vol. 18, no. 11, p. 2465, 2025.

[5] M. Sonmez *et al.*, "Development, Testing, and Thermoforming of Thermoplastics Reinforced with Surface-Modified Aramid Fibers for Cover of Electronic Parts in Small UAVs," *Polymers*, vol. 16, no. 15, p. 2136, 2024.

[6] Y. Nurgizat, A. Uzbekbayev, I. Fedorov, A. Bebenin, and A. Karypov, "Structural and Material Optimization of a Sensor-Integrated Autonomous Aerial Vehicle Using KMU-3 CFRP," *Polymers*, vol. 17, no. 16, p. 2175, 2025.

[7] N. Tiruvenkadam, S. Shankar, P. Kumar, and S. Gowtham, "Investigation of Structural and Thermal Analysis of Drone Propeller Materials," *J. Phys.: Conf. Ser.*, vol. 2925, p. 012002, 2024.

[8] S. Chevula, S. Chillamcharal, and S. Maddula, "A Computational Design Analysis of UAV's Rotor Blade in Low-Temperature Conditions," *Int. J. Aerosp. Eng.*, vol. 2021, p. 8843453, 2021.

[9] J. P. V. S. Nathan *et al.*, "Operation of Advanced Flying Wing UAV: Structural Performance under Aberrant Pressure and Thermal Loading," *SAE Tech. Paper Ser.*, 2025.

[10] A. Vedrtnam, H. Negi, and K. Kalauni, "Materials and Energy-Centric Life Cycle Assessment for Drones: A Review," *J. Compos. Sci.*, vol. 9, no. 4, p. 169, 2025.

[11] D. Häusermann *et al.*, "FireDrone: Multi-Environment Thermally Agnostic Aerial Robot," *Adv. Intell. Syst.*, vol. 5, p. 2300101, 2023.

[12] N. M. Maity, "Lightweight Thermal Insulation Systems in Medical Delivery Drones," *IEEE Aerosp. Conf.*, pp. 1–7, 2021.

[13] Y. Chen *et al.*, "Ceramic Fiber-Functionalized Silica Aerogel Coating for Lightweight Thermal Protection of UAVs in Extreme Environments," *J. Am. Ceram. Soc.*, vol. 109, p. 70720, 2026.

[14] J. Ding *et al.*, "A novel lightweight ceramizable Si-B hybrid phenolic aerogel composite with excellent thermal insulation and ablation resistance," *Nanoscale*, 2026.

[15] X. Chang *et al.*, "Multiphase Symbiotic Engineered Elastic Ceramic-Carbon Aerogels with Advanced Thermal Protection in Extreme Oxidative Environments," *Adv. Mater.*, vol. 36, p. 2406055, 2024.

[16] J. Li *et al.*, "Fabrication of Large Aerogel-Like Carbon/Carbon Composites with Excellent Load-Bearing Ca-

pacity and Thermal-Insulating Performance at 1800 °C," *ACS Nano*, vol. 16, 2022.

[17] H. Wang *et al.*, "Gradient fiber-reinforced aerogel composites using surface ceramicizable-resin densification with outstanding ablation resistance," *Compos. Sci. Technol.*, vol. 228, p. 109798, 2022.

[18] X. Hou *et al.*, "Thermal Insulation and Fireproof Aerogel Composites for Automotive Batteries," *Gels*, vol. 11, no. 10, p. 791, 2025.

[19] X. Jiang, Y. Guo, and Y. Zhou, "Research Progress on Thermal Insulation Material Systems for High-Speed Aircrafts," *Materials*, vol. 19, no. 7, p. 1311, 2026.

[20] T. Yanko, R. Datsenko, and H. Karpenko, "Possibilities of Using Low-Density C–C Composites for Thermal Protection of Small Unmanned Aerial Vehicles," *Trans. Aerosp. Res.*, vol. 2023, pp. 45–57, 2023.

[21] B. Liu *et al.*, "Materials design of silicon based ceramic coatings for high temperature oxidation protection," *Mater. Sci. Eng. R*, vol. 162, p. 100936, 2025.

[22] S. Ren, Y. Sun, H. Yan, X. Zhang, Y. Bao, and K. Lv, "A Review on the Evolution of Thermal and Environmental Barrier Coating Systems and Their High-Temperature Degradation Mechanisms in Advanced Aero-Engines," *Materials*, vol. 19, no. 11, p. 2413, 2026.

[23] Q. Cao, I. Oluwoye, T. Pojtanabuntoeng, H. Farhat, and M. Iannuzzi, "Evaluation of epoxy-based coating degradation under thermal insulation at elevated temperatures on different steel substrates," *Prog. Org. Coat.*, vol. 180, p. 107544, 2023.

[24] D. He, F. Jiao, D. Ou, H. Gao, and J. Wu, "Thermal insulation and anti-vibration properties evaluation of modified epoxy resin-based thermal protection coatings in arc-jet," *Prog. Org. Coat.*, vol. 172, p. 107158, 2022.

[25] S. Shi *et al.*, "Thermal decomposition behavior of a thermal protection coating composite with silicone rubber: Experiment and modeling," *Prog. Org. Coat.*, vol. 143, p. 105609, 2020.

[26] Z. Fan *et al.*, "Thermal protective and hydrophobic coating on polyimide resin matrix composites surface for improved aging resistance," *Polym. Compos.*, 2024.

[27] G. Pamula and A. Ramachandran, "Thermal Management for Unmanned Aerial Vehicle Payloads: Mechanisms, Systems, and Applications," *Drones*, vol. 9, no. 5, p. 350, 2025.

[28] J. Huang, W. Sun, Z. Zhang, Z. Ling, and X. Fang, "Thermal protection of electronic devices based on thermochemical energy storage," *Appl. Therm. Eng.*, vol. 186, p. 116507, 2021.